

Exploring the distinction between experimental resonant modes and theoretical eigenmodes: From vibrating plates to laser cavities

P. H. Tuan,¹ C. P. Wen,¹ Y. T. Yu,¹ H. C. Liang,² K. F. Huang,¹ and Y. F. Chen^{1,*}

¹Department of Electrophysics, National Chiao Tung University, 1001 Ta-Hsueh Road, Hsinchu 30010, Taiwan

²Institute of Optoelectronic Science, National Taiwan Ocean University, Keelung 20224, Taiwan

(Received 19 November 2013; revised manuscript received 14 January 2014; published 12 February 2014)

Experimentally resonant modes are commonly presumed to correspond to eigenmodes in the same bounded domain. However, the one-to-one correspondence between theoretical eigenmodes and experimental observations is never reached. Theoretically, eigenmodes in numerous classical and quantum systems are the solutions of the homogeneous Helmholtz equation, whereas resonant modes should be solved from the inhomogeneous Helmholtz equation. In the present paper we employ the eigenmode expansion method to derive the wave functions for manifesting the distinction between eigenmodes and resonant modes. The derived wave functions are successfully used to reconstruct a variety of experimental results including Chladni figures generated from the vibrating plate, resonant patterns excited from microwave cavities, and lasing modes emitted from the vertical cavity.

DOI: 10.1103/PhysRevE.89.022911

PACS number(s): 05.45.Mt, 02.30.Mv, 42.55.Px, 46.40.Ff

I. INTRODUCTION

Eigenfrequencies and eigenmodes are fundamental elements in studying classical and quantum wave systems such as electromagnetic waveguides [1], acoustic vibrators [2], optical cavities [3,4], and quantum billiards [5]. Eigenmodes of the bounded wave systems are generally associated with the homogeneous Helmholtz equation with boundary conditions [6–8]. Two-dimensional (2D) scientific systems such as microwave cavities [9,10], vibrating plates [11], oscillating water tanks [12], and laser resonators [13,14] have been extensively employed to generate wave patterns of resonant modes that are presumed to be the experimental observations for theoretical eigenmodes. However, it is frequently found that there are significant discrepancies between theoretical eigenmodes and experimental observations in the one-to-one correspondence [15–18]. The deviation between resonant modes and theoretical eigenmodes can be traced back to experimental studies of free vibrating plates [15,16]. Experimental results indicate that the compounded modes instead of eigenmodes are usually generated in the vibrating plates owing to the effects of degeneracy and damping. Moreover, numerous results of research [18–20] also reveal that external parameters such as the driven source and measuring device can cause the resonant modes to display various eigenmode-mixing phenomena. Scattering theory [21,22] has been used to study the frequency spectra and spatial patterns in microwave cavities because the entering and measuring antennas take the role of the scattering channels. However, for other experimental systems such as laser resonators and vibrating plates, the spatial patterns of resonant modes can be measured with the straightforward imaging method instead of the invasive scattering process. For such resonant systems, a detailed exploration to analyze the spatial morphologies of resonant modes and to make a connection between experimental resonant modes and theoretical eigenmodes is lacking.

From a theoretical point of view, the resonant modes of a confined system driven by a localized source should

be analyzed by means of the inhomogeneous Helmholtz equation with the corresponding boundary condition. The inhomogeneous Helmholtz equation in electrodynamics is frequently used to analyze the free-space propagation of the time-harmonic wave. Nevertheless, it remains an interesting issue whether the inhomogeneous Helmholtz equation can be exploited to interpret the spatial patterns observed from the resonant systems with direct imaging.

In this work we employ the eigenmodes of a 2D confined system with a boundary condition as the basis to derive an analytical representation for the resonant modes of the inhomogeneous Helmholtz equation with the same bounded domain. The expansion method enables us to express the resonant modes as the superposition of eigenmodes with precise weighting coefficients that are clearly associated with the degeneracy, source position, and damping effects. We utilize the derived expression to analyze a variety of resonant nodal-line patterns observed in the famous Chladni experiment for a square plate with different source locations. All experimental patterns are found to be excellently reconstructed with the calculated resonant modes. To further manifest the distinction between experimental resonant modes and theoretical eigenmodes, we exploit the wave functions for the resonant modes to reconstruct the experimental patterns in microwave resonators as well as vertical-cavity surface-emitting lasers (VCSELs). The striking agreement manifests the significance of the resonant modes in interpreting the experimental results.

II. DISTINCTION BETWEEN RESONANT MODES AND EIGENMODES

In general, the eigenvalues k_n and normalized eigenmodes φ_n of a 2D confined system, such as quantum billiards, a disk resonator, and a vibrating plate, can be obtained from the homogeneous Helmholtz equation

$$(\nabla^2 + k_n^2)\varphi_n(x, y) = 0, \quad (1)$$

with fixed $\Psi|_{\partial\Omega} = 0$ (Dirichlet) or free $\partial\Psi/\partial n|_{\partial\Omega} = 0$ (Neumann) boundary condition, where $\partial\Omega$ is the boundary of the confinement. The resonant mode $\Psi(x, y; \tilde{k})$ in the same bounded domain can be solved from the inhomogeneous

*yfchen@cc.nctu.edu.tw

Helmholtz equation

$$(\nabla^2 + \tilde{k}^2)\Psi(x, y; \tilde{k}) = F(x, y), \quad (2)$$

where $F(x, y)$ is the distribution of the driven source and \tilde{k} is the complex wave number. To consider the system dissipation, we express the complex wave number as $\tilde{k} = k + i\gamma$, where k is the wave number related to the driven frequency and γ is the damping factor for characterizing the cavity losses. With the expansion of normalized eigenmodes, the resonant mode and the source distribution can be expressed as the superposition of eigenmodes

$$\Psi(x, y; \tilde{k}) = \sum_n a_n(\tilde{k})\varphi_n(x, y) \quad (3)$$

and

$$F(x, y) = \sum_n f_n \varphi_n(x, y). \quad (4)$$

Substituting Eqs. (2) and (3) into Eq. (1), the orthonormal property of eigenmodes can be used to obtain the relationship between coefficients a_n and f_n :

$$a_n = f_n / (\tilde{k}^2 - k_n^2). \quad (5)$$

The damping factor γ is considerably smaller than the wave number k for most resonant systems. As a result, the resonant mode can be given by

$$\Psi(x, y; k, \gamma) = \sum_n \frac{f_n}{(k^2 - k_n^2) + 2i\gamma k} \varphi_n(x, y), \quad (6)$$

where

$$f_n = \iint \varphi_n^*(x, y) F(x, y) dx dy. \quad (7)$$

For the system driven by a pointlike source at the location of (x', y') , the resonant mode in Eq. (6) can be explicitly expressed as

$$\Psi(x, y; k, \gamma) = \sum_n \frac{\varphi_n^*(x', y')}{(k^2 - k_n^2) + 2i\gamma k} \varphi_n(x, y). \quad (8)$$

Equation (8) clearly reveals that the resonant mode is mainly contributed by the eigenmodes satisfying two criteria. First, in the denominator, the eigenfrequencies k_n need to be fairly close to the driven frequency k ; second, in the nominator, the eigenmodes φ_n require one to contribute a sufficient amplitude at the excitation position (x', y') . In contrast, the damping factor γ determines the effective resonance width of the system and leads to the presence of overlapping resonance. Since $|a_n|^2$ is the relative probability of the resonant mode $\Psi(x, y; k, \gamma)$ in the eigenstate $\varphi_n(x, y)$, the resonance strength can be evaluated from the total summation $\sum_n |a_n|^2$. For the resonant modes in Eq. (8), the resonance strength can be given by

$$I(x', y', k, \gamma) = \sum_n \frac{|\varphi_n(x', y')|^2}{[(k^2 - k_n^2)^2 + 4(\gamma k)^2]}. \quad (9)$$

We use Eq. (8) to calculate the spatial morphologies of the resonant modes in the square and quarter-stadium billiards to demonstrate the role of degeneracy and damping. The driven source is set at the center of mass of the billiards. Figures 1(a)

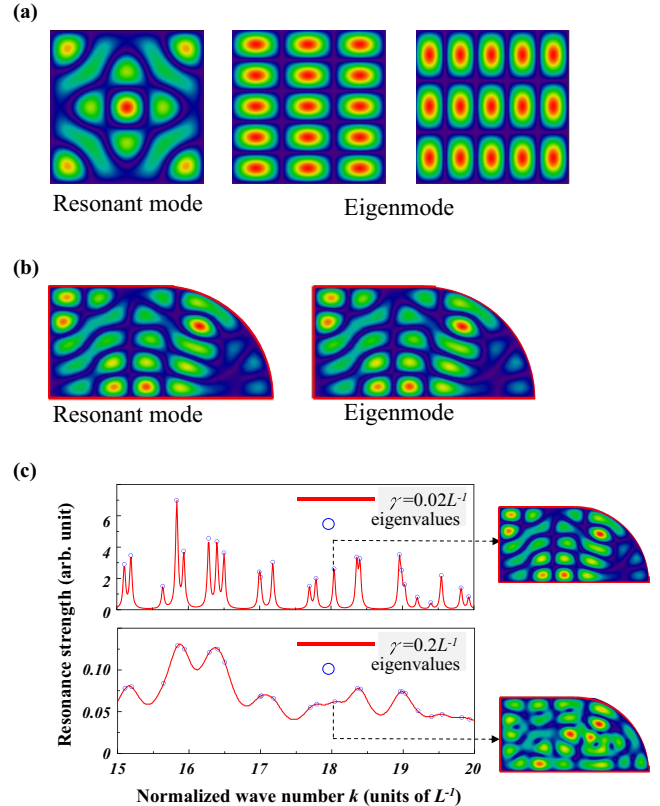


FIG. 1. (Color online) Resonant mode and eigenmode of (a) square billiards with normalized $k = 18.318L^{-1}$ and $\gamma = 0.02L^{-1}$ and (b) quarter-stadium billiards with normalized $k = 18.042L^{-1}$ and $\gamma = 0.02L^{-1}$. (c) Resonance strengths with different damping factor and their corresponding resonant patterns in quarter-stadium billiards.

and 1(b) show the numerical patterns for the square billiards with $k = 18.318L^{-1}$ and the quarter-stadium billiards with $k = 18.042L^{-1}$, where a small damping factor of $\gamma = 0.02L^{-1}$ is used in the calculation and L is the longest axis of the billiards. As shown in Fig. 1(a), the property of level clustering in the square billiards [23] can cause the resonant mode to be superposed by several degenerate eigenmodes. In contrast, the effect of level repulsion in the quarter-stadium billiards [24] can guarantee the resonant mode to be nearly the same as the eigenmode in the isolated resonance region, as depicted in Fig. 1(b). To demonstrate the influence of the damping effect on the overlapping resonance, we use Eq. (9) to calculate the resonance strength of the quarter-stadium billiards in the range of $k = 15L^{-1}-20L^{-1}$. Figure 1(c) shows the calculated results for the two cases $\gamma = 0.02L^{-1}$ and $0.2L^{-1}$. It is clear that when the damping factor γ is greater than the mean level spacing, the overlapping resonance can induce an additional mode-mixing phenomenon.

Note that even though Eq. (9) may be used to estimate the resonance frequencies, this formula does not consider the effect of leading to a shift of resonances. It has been found [21] that the influence of surrounding noise or internal perturbation can cause a shift of resonances. Nevertheless, the next verification reveals that Eq. (8) can successfully be exploited to reconstruct the experimental resonant mode

with a best-fit wave number that is determined by searching for the calculated pattern that most closely resembles the experimental result in the vicinity of the unperturbed resonance. In the following, we will make a thorough comparison between the numerical calculation and the experimental observation to manifest the importance of the resonant modes.

III. RECONSTRUCTION OF EXPERIMENTAL RESONANT MODES

A. Chladni figures in square vibrating plates

We employ the classical Chladni figures in square vibrating plates to verify the usefulness of the resonant modes. In the experimental setup, we load the center of a square plate on a mechanical vibrator with the oscillating frequency from 0 to 6 kHz under sinusoidal wave operation. The mechanical vibrator is connected to a function generator with a 1.0-W amplifier. With silica sand uniformly distributed on the vibrating plate, the resonant modes can be clearly observed through direct imaging for the nodal patterns forming in the

sand when the driven frequency is close to one of the resonant frequencies. The square plate is fabricated by aluminum with a side length $a = 240$ mm and uniform thickness $d = 1$ mm. By continuously changing the frequency of the vibrator, we record a series of nodal-line patterns with stable structures. The experimental nodal-line patterns can be classified into three categories, as shown in Figs. 2(a), 3(a), and 4(a), respectively.

In the theoretical calculation, we assume a free (Neumann) boundary condition for the system. Since the ratio $a/d = 240$ is rather large, the vibrating behavior of the square plate is similar to a square membrane, which can be simply described by the Helmholtz equation [25]. Consequently, the eigenmodes and eigenvalues of the square plate can be in terms of two integer indices m and n :

$$\varphi_{m,n}(x,y) = \frac{2}{a} \cos\left(\frac{m\pi}{a}x\right) \cos\left(\frac{n\pi}{a}y\right) \quad (10)$$

and

$$k_{m,n} = \frac{\pi}{a} \sqrt{m^2 + n^2}. \quad (11)$$

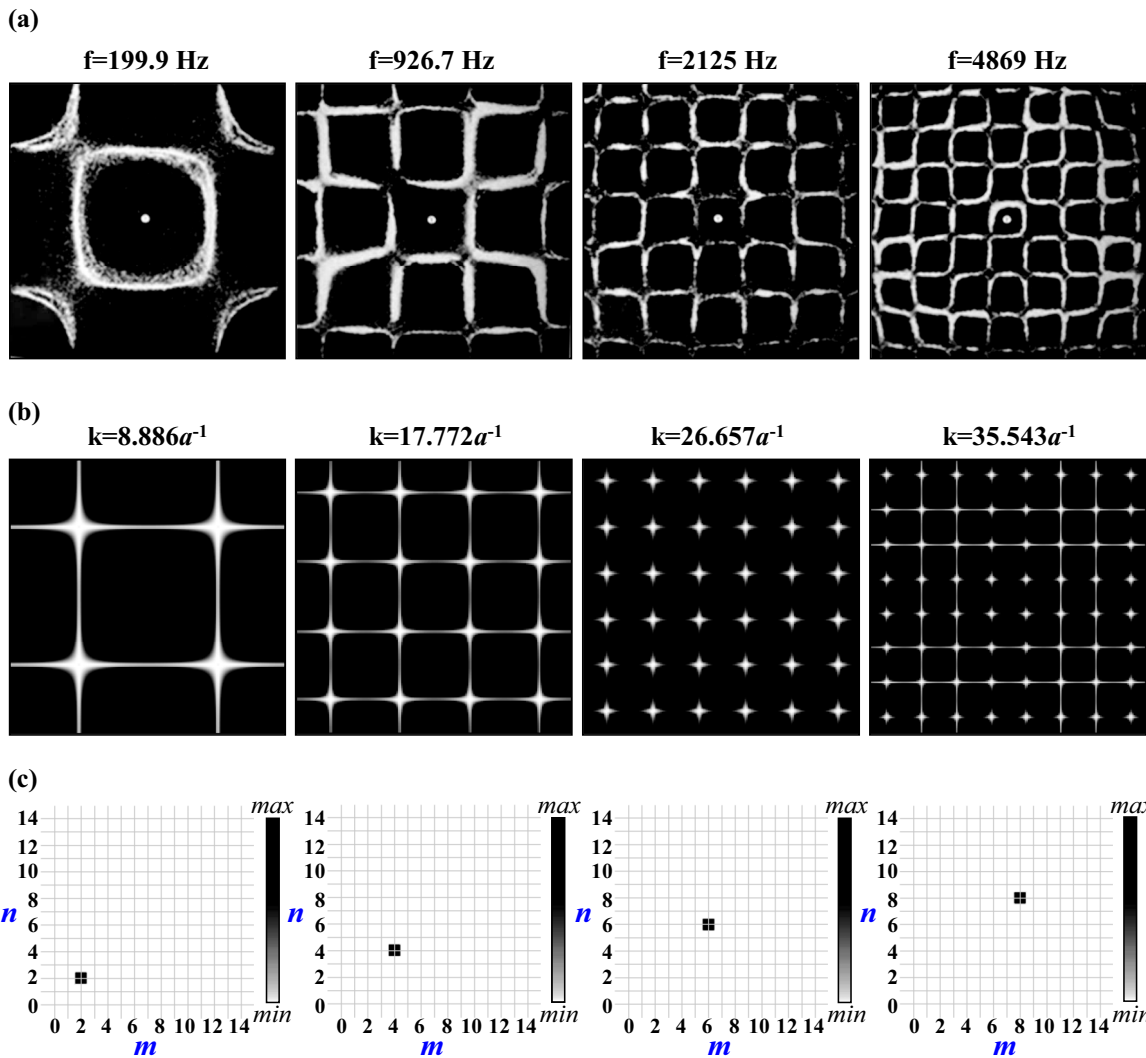


FIG. 2. (Color online) First category of resonant modes for a square plate under the central excitation condition: eigenmodes with $m = n$. (a) Experimental nodal-line patterns. (b) Calculated results. (c) Eigenmode composition with a normalized color bar.

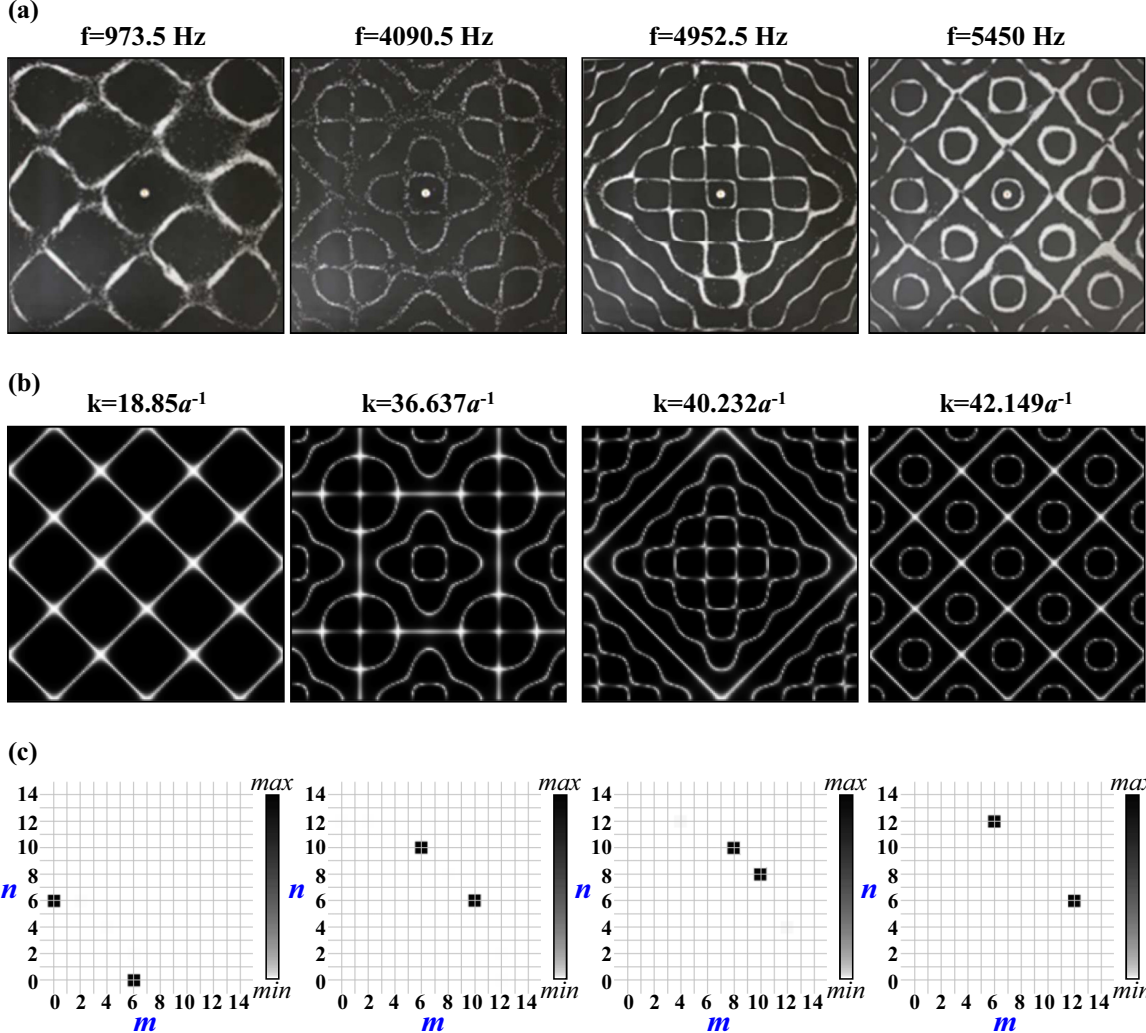


FIG. 3. (Color online) Second category of resonant modes for a square plate under the central excitation condition: normal modes with exact degeneracy. (a) Experimental nodal-line patterns. (b) Calculated results. (c) Eigenmode composition with a normalized color bar.

With Eq. (8), the resonant modes of the square plate under point-source excitation can be expressed as

$$\Psi(x, y; k, \gamma) = \left(\frac{2}{a}\right)^2 \sum_m \sum_n \frac{\cos\left(\frac{m\pi}{a}x'\right) \cos\left(\frac{n\pi}{a}y'\right)}{(k^2 - k_{m,n}^2) + 2i\gamma k} \times \cos\left(\frac{m\pi}{a}x\right) \cos\left(\frac{n\pi}{a}y\right). \quad (12)$$

To compare with the experimental results, we use $\gamma = 0.02a^{-1}$ in Eq. (12) for the calculation. The value of the damping factor γ is determined from the best fit to the experimental results. Figures 2(b), 3(b), and 4(b) show the calculated results for the nodal-line patterns corresponding to the experimental observations shown in Figs. 2(a), 3(a), and 4(a), respectively. It can be seen that the numerical nodal-line patterns agree very well with the experimental results for all cases.

With Eq. (12), the eigenmode composition for each resonant mode can be explicitly evaluated. Figures 2(c), 3(c), and 4(c) depict the eigenmode compositions for three categories of resonant modes shown in Figs. 2(b), 3(b), and 4(b), respec-

tively. Since the pointlike driven source is located at the center of the square plate, the weighting coefficients for the composed eigenmodes can be found to be symmetrically distributed along the line of $m=n$ on the plane of the indices m and n . The first kind of resonant mode shown in Fig. 2 can be found to be just the pure eigenmodes $\varphi_{m,n}(x, y)$ with $m=n$. The second case shown in Fig. 3 is the general normal mode that is superposed by two eigenmodes of $\varphi_{m,n}(x, y)$ and $\varphi_{n,m}(x, y)$. The third category shown in Fig. 4 is the so-called compounded normal mode [15,16] that is formed by numerous eigenmodes satisfying the nearly degenerate condition of $k_{m,n} \approx \text{const}$, i.e., $m^2 + n^2 \approx \text{const}$. Note that the generation of compounded normal modes comes from the accidental degeneracy as well as the damping effect. Moreover, in there are no convincing theoretical explanations for the nodal-line patterns of compound normal modes.

The comparison made above focuses mainly on the experiment with the driven source at the central position of $(a/2, a/2)$. For many other resonant systems, it has been demonstrated that a minute asymmetry and boundary

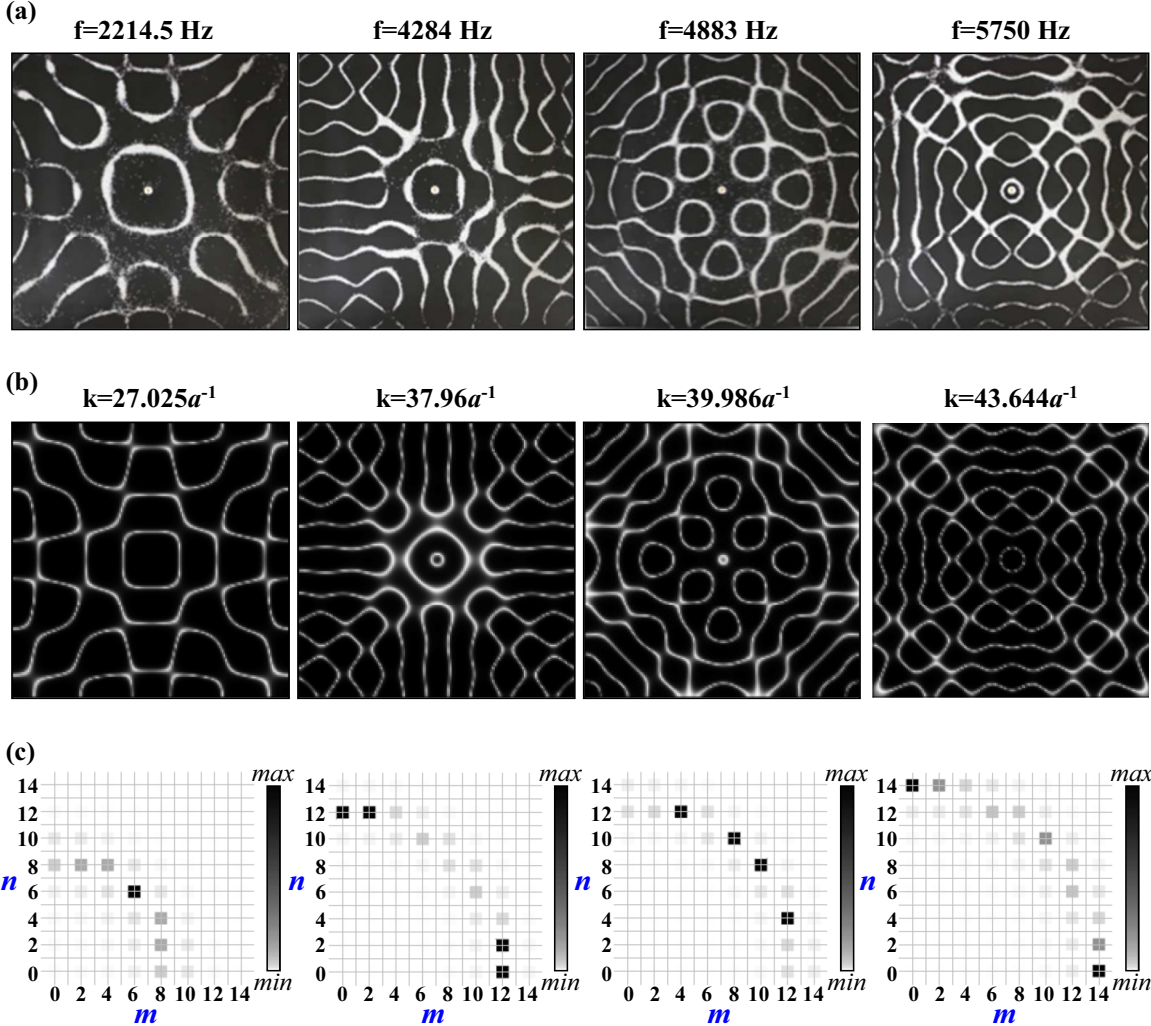


FIG. 4. (Color online) Third category of resonant modes for a square plate under the central excitation condition: compounded normal modes with near degeneracy. (a) Experimental nodal-line patterns. (b) Calculated results. (c) Eigenmode composition with a normalized color bar.

roughness can lead to more complicated patterns [26,27] as well as the chaotic nodal domains [28,29]. To further validate the theoretical model and the asymmetry effect, we perform the experiment of the square vibrating plate with the driven source off the central position. In this experiment, we shift the driven source from the center of the square plate with a small distance of $0.013a$ along the direction at an angle 67° with respect to the x axis. Figure 5(a) shows experimental results for the nodal-line patterns with irregular characteristics. Substituting the source position and $\gamma = 0.02a^{-1}$ into Eq. (12), the theoretical patterns are calculated. Figures 5(b) and 5(c) depict, respectively, the numerical nodal-line patterns and the eigenmode compositions corresponding to the experimental results shown in Fig. 5(a). Once again, the numerical patterns are in good agreement with the experimental observations. The good agreement validates the applicability of the theoretical model for analyzing the spatial morphologies of resonant modes. As seen in Fig. 5(c), the resonant modes generated with an off-center excitation are formed by the superposition of nearly degenerate eigenmodes and the weighting coefficients lose the symmetry discussed in the case of central driving.

B. Resonant patterns in microwave cavities

Microwave resonators are now widely used to explore the properties of high-order wave functions in quantum (wave) billiards. However, as mentioned in the Introduction, experimental observations are of the resonant modes instead of the eigenmodes. In this section we employ the developed model to analyze the experimental wave patterns in the rectangular microwave cavity [18]. For the rectangular microwave cavity excited with a pointlike antenna at (x', y') , Eq. (6) can be used to express the resonant mode as

$$\Psi(x, y; k, \gamma) = \frac{4}{ab} \sum_{m=1}^{\infty} \sum_{n=1}^{\infty} \frac{\sin\left(\frac{m\pi}{a}x'\right) \sin\left(\frac{n\pi}{b}y'\right)}{(k^2 - k_{m,n}^2) + 2i\gamma k} \times \sin\left(\frac{m\pi}{a}x\right) \sin\left(\frac{n\pi}{b}y\right), \quad (13)$$

where $k_{m,n} = \pi\sqrt{(m/a)^2 + (n/b)^2}$, a and b are the side lengths, and k is the wave number of the excitation source. Using Eq. (13) and the information of the experimental setup, i.e., $a = 340$ mm, $b = 240$ mm, $x' = 250$ mm,

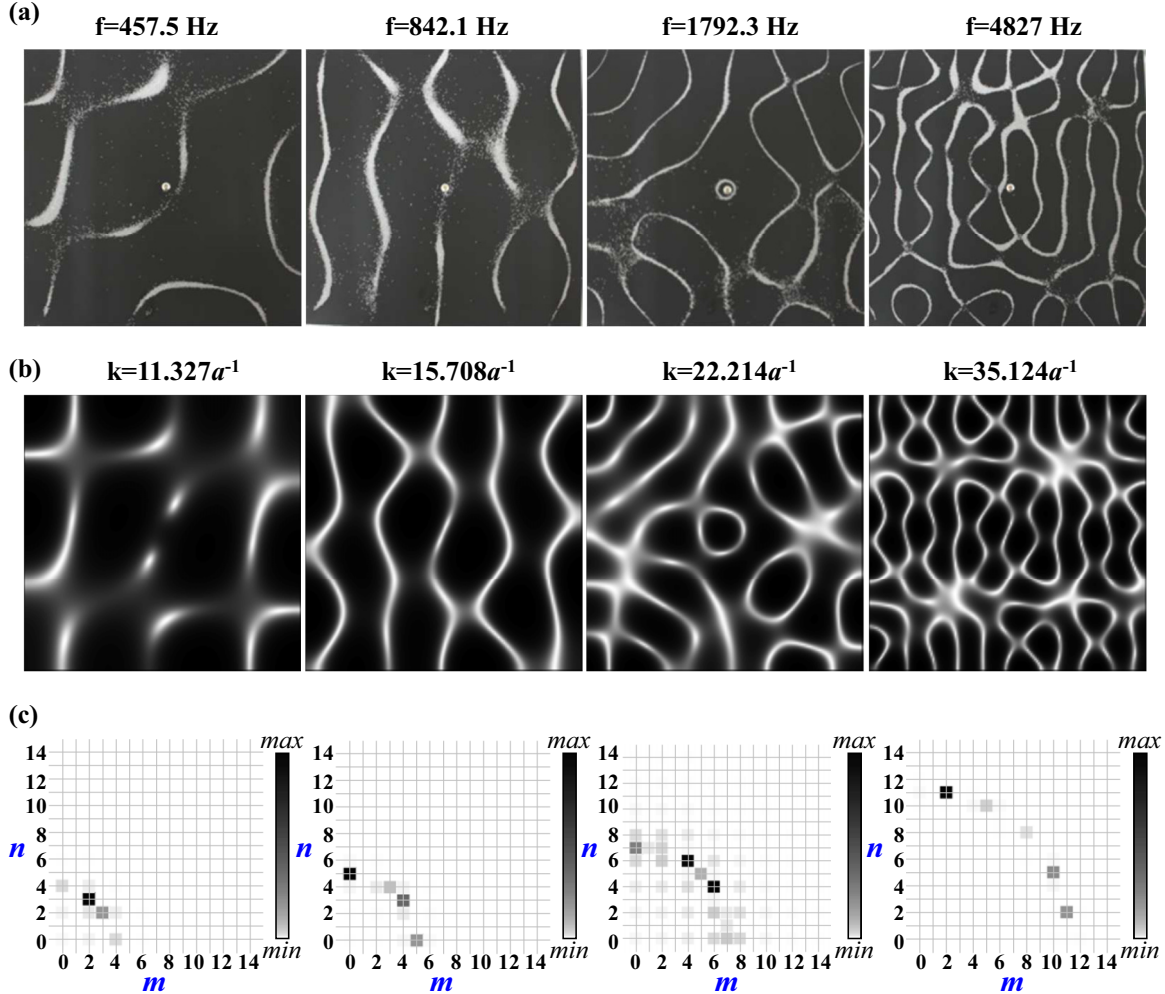


FIG. 5. (Color online) (a) Experimental nodal-line patterns generated by the asymmetrical excitation. (b) Calculated results. (c) Eigenmode composition with a normalized color bar.

$y' = 140$ mm, and $\gamma = 0.005a^{-1}$ [18], the theoretical wave patterns can be systematically calculated in the vicinity of the resonance frequencies. Figure 6 shows the comparison between the experimental patterns (left column) and the numerical calculations (right column) for the resonant wave numbers at (a) $k = 16.29a^{-1}$, (b) $k = 16.34a^{-1}$, (c) $k = 17.99a^{-1}$, (d) $k = 18.06a^{-1}$, (e) $k = 23.11a^{-1}$, and (f) $k = 23.15a^{-1}$. It is clear that the numerical patterns agree very well with the experimental measurements.

In most experiments of microwave billiards, the antennas frequently arouse the effect of pointlike perturbations, which may significantly influence the structures of the resonant modes in the cavity. To take the scattering effect into account, we add in a finite-size circular scatter with radius $r = 0.005a$ at the center of cavity and employ the developed expression to explore the resonant modes once again. If we assume that the microwave is totally reflected at the inner scatter, the Dirichlet condition is imposed on the boundary of scatter to solve the wave functions. To construct the resonant modes of this non-integrable Sinai-like billiards, we first exploit the expansion method [6] to evaluate the eigenvalues k_n and eigenmodes $\varphi_n(x,y)$ under this geometry as a quasicomplete basis. The

detailed mathematics are similar as the derivation in Ref. [30]. Substituting the solved eigenvalues k_n and eigenmodes $\varphi_n(x,y)$ into Eq. (8) under the same point-excitation position and damping factor as before, we construct the resonant modes from a low-order regime to a high-order regime with the effective wavelength $2\pi/k = \lambda_{\text{eff}} = 0.24a - 0.07a$. Figure 7 shows the resonant modes of the microwave cavity with and without the inner scatter. The wave numbers for each case from the top to the bottom are $k = 26.60a^{-1}$, $28.29a^{-1}$, $41.13a^{-1}$, $45.65a^{-1}$, $82.65a^{-1}$, and $125.50a^{-1}$, respectively. Because the radius of scatter is considerably smaller than λ_{eff} for the low-order states, the effect of pointlike perturbation is extremely weak and leaves the structures of the resonant modes nearly unchanged. However, as λ_{eff} gradually decreases and approximates to the scale of inner scatter, the pointlike perturbation exhibits a drastic scattering effect resulting in significant change in the structures of resonant modes. This numerical discussion not only shows the feasibility of the developed expression to analyze the resonant mode for the microwave systems under pointlike perturbation but also sheds light on the exploration of the resonant mode in systems with even more complicated coupling effects, e.g., the laser cavity.

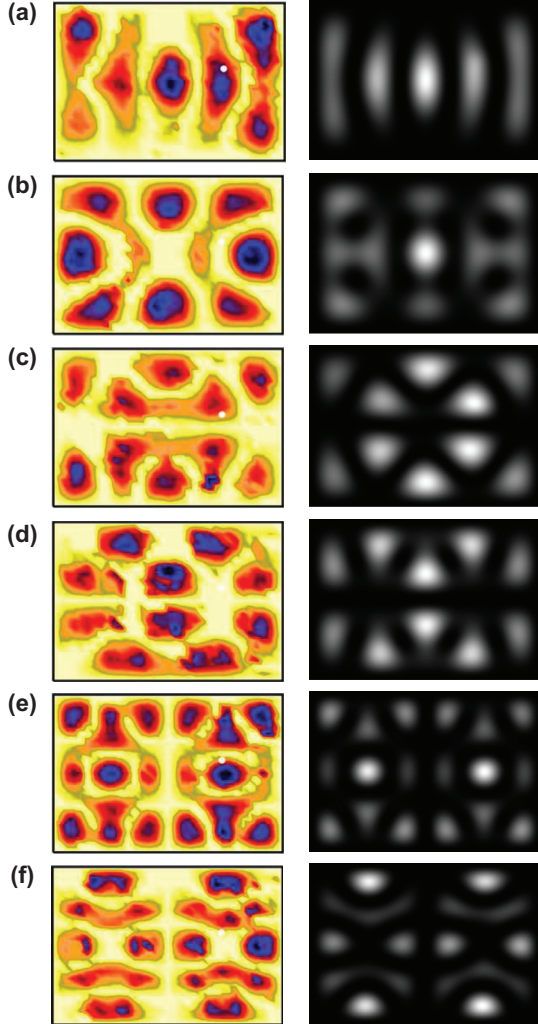


FIG. 6. (Color online) Comparison between experimental observations (left column) [18] and numerical patterns (right column) for the resonant modes at wave numbers (a) $k = 16.29a^{-1}$, (b) $k = 16.34a^{-1}$, (c) $k = 17.99a^{-1}$, (d) $k = 18.06a^{-1}$, (e) $k = 23.11a^{-1}$, and (f) $k = 23.15a^{-1}$.

C. Lasing modes in VCSELs

Optical microcavities have great potential for applications in miniature lasers, biological sensors, optical telecommunications, and basic research in modern physics [31–35]. Large-aperture oxide-confined VCSELs, serving as an analogous quantum billiards, have been employed to explore quantum wave functions in mesoscopic systems [35,36]. Because of the extremely short cavity length, VCSELs inherently emit a single-longitudinal-mode light wave with a predominantly propagating wave number. In contrast, the large discontinuities between the current-guiding oxide layer and the semiconductor gain materials ensure that the light wave undergoes total internal reflection at the boundary of transverse confinement. As a consequence, the VCSEL cavity can be considered as a planar waveguide with a dominant wave vector along the longitudinal direction [13,17].

According to the waveguide theory [37], the light fields with a wave vector k_z predominantly propagating along the

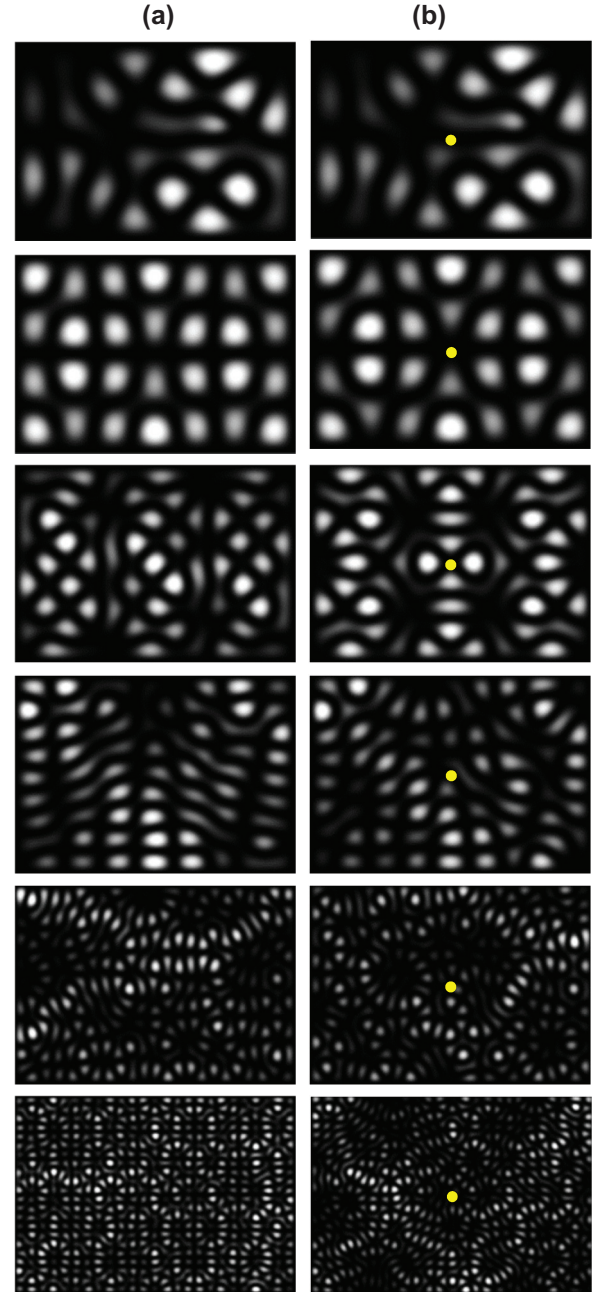


FIG. 7. (Color online) Comparison between the numerical resonant modes in the microwave cavity from the low-order regime to the high-order regime (a) without and (b) with a pointlike perturbation marked by the yellow (white) solid circle. The wave numbers are (from top to bottom) $k = 26.60a^{-1}$, $28.29a^{-1}$, $41.13a^{-1}$, $45.65a^{-1}$, $82.65a^{-1}$, and $125.50a^{-1}$.

z direction in a uniform medium can be approximated as $E(x, y, z) = \varphi(x, y)e^{i(k_z - \omega t)}$, where ω is the angular frequency. By substituting the expression into the Maxwell equations one will reach the 2D Helmholtz equation as depicted by Eq. (1) with transverse wave number $k_n^2 = \omega^2/c^2 - k_z^2$. Some of the lasing modes in VCSELs corresponding to the superscarred wave functions have been observed and explained by a coherent superposition of eigenmodes [17,36]. Nevertheless, the lasing modes in VCSELs should correspond to the resonant

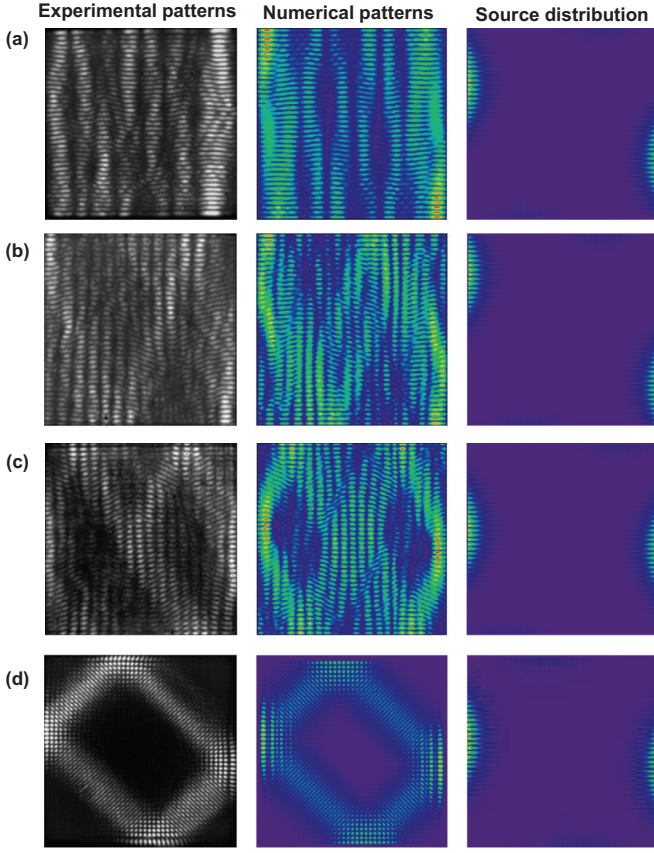


FIG. 8. (Color online) Comparison between experimental lasing modes (left column) and numerically reconstructed resonant modes (middle column) with the corresponding source distributions (right column). The parameters (ξ , η , k) are for patterns (a) ($-0.2a$, $0.2a$, $127.8a^{-1}$), (b) ($-0.3a$, $0.2a$, $140.7a^{-1}$), (c) ($-0.05a$, $0.3a$, $146.9a^{-1}$), and (d) ($-0.07a$, $-0.1a$, $184.4a^{-1}$).

modes instead of the eigenmodes. Here we try to reconstruct the lasing modes emitted from the large-aperture square VCSEL with the resonant modes in Sec. II. In general, the transverse orders of the lasing modes can be varied via detuning of the device temperature. The first column of Fig. 8 depicts four typical lasing patterns observed in the square VCSELs near threshold with an aperture size of $40 \times 40 \mu\text{m}^2$. The device structure of the oxide-confined VCSEL is similar to those described in Ref. [33]. It can be seen that the lasing mode displays a pattern changing from the quasiperiodic linear ridge to the diamond-shaped feature for operation temperature decreasing from 298 to 180 K.

With the square-billiard model, the eigenmodes for the large-aperture square VCSEL can be given by

$$\varphi_{m,n}(x,y) = \frac{2}{a} \sin\left[\frac{m\pi}{a}\left(x + \frac{a}{2}\right)\right] \sin\left[\frac{n\pi}{a}\left(y + \frac{a}{2}\right)\right], \quad (14)$$

where the mode region is defined to be in the range of $|x| \leq a/2$ and $|y| \leq a/2$, a is the side length of the active area, and m and n are the positive integers for the mode indices. Since it is difficult to determine the source distributions for the VCSELs with a theoretical approach, we use a phenomenological way with minimum fitting parameters to reconstruct the experimental patterns. Based on the fact that the pump current

is injected from the outside edge of the lateral periphery, the source distribution perpendicular to the sidewall toward the center is modeled as an exponential decay. In contrast, the excitation source parallel to the sidewall is modeled as a Gaussian distribution with sinusoidal modulation. The sinusoidal modulation is used to consider the effect of spatial hole burning. The source distribution for the square VCSEL is explicitly given by

$$F(x,y) = A[g_+(x,y;\xi)g_-(x,y;\xi)] + B[h_+(x,y;\eta) + h_-(x,y;\eta)], \quad (15)$$

with

$$g_{\pm}(x,y;\xi) = \exp\left(-\frac{|x \pm (a/2)|}{d}\right) \exp\left(-\frac{(y \pm \xi)^2}{\omega^2}\right) \times \sin\left[\frac{s\pi}{a}\left(y + \frac{a}{2}\right)\right] \quad (16)$$

and

$$h_{\pm}(x,y;\eta) = \exp\left(-\frac{|y \pm (a/2)|}{d}\right) \exp\left(\frac{(x \pm \eta)^2}{\omega^2}\right) \times \sin\left[\frac{s\pi}{a}\left(x + \frac{a}{2}\right)\right], \quad (17)$$

where A and B are the weighting factors for the relative intensities along the x and y directions, respectively, d is the parameter for the exponential decay, ω is the effective width for the Gaussian distribution, ξ and η are the parameters for the center positions of the Gaussian distribution, and s is the parameter for the sinusoidal modulation. To reconstruct the experimental patterns shown in Fig. 8, we numerically confirm that only the parameters (ξ , η , k) need to be varied and the values for other parameters can be fixed: $A = 1.0$, $B = 0.1$, $d = a/20$, $\omega = a/5$, and $s = 41$. The parameters (ξ , η , k) for the patterns in Figs. 8(a)–8(d) are numerically found to be ($-0.2a$, $0.2a$, $127.8a^{-1}$), ($-0.3a$, $0.2a$, $140.7a^{-1}$), ($-0.05a$, $0.3a$, $146.9a^{-1}$), and ($-0.07a$, $-0.1a$, $184.4a^{-1}$), respectively. Numerically reconstructed patterns and corresponding excitation sources are shown in the second and third columns of Fig. 8, respectively. In order to quantitatively analyze the correlation between experimental and numerical resonant modes with complex structures, we further calculate the spatial correlation function given by $C(\vec{\tau}) = \int f(\vec{r} + \vec{\tau})g(\vec{r})d\vec{r}$, where $f(\vec{r} + \vec{\tau})$ and $g(\vec{r})$ are normalized functions of the spatial coordinates. Two spatial functions are regarded as being highly related as the value of $C(\vec{\tau})$ approaches one. The calculated values of $C(\vec{\tau})$ for the cases in Fig. 8 are as follows: (a) 0.84, (b) 0.87, (c) 0.81, and (d) 0.83. The high values of $C(\vec{\tau})$ show that the experimental patterns can be nicely reconstructed with the resonant modes and numerical analysis. Once again, the good agreement not only manifests the distinction between the resonant modes and eigenmodes in the bound-state problems but also confirms the significance of the resonant modes in interpreting the experimental results.

IV. CONCLUSION

With the inhomogeneous Helmholtz equation and the expansion method of eigenmodes, we have derived the wave function of the resonant mode as a superposition of eigenmodes in the 2D confined system. The derived expression clearly discloses the effects of degeneracy and damping on the formation of resonant modes. A variety of Chladni figures generated from the square vibrating plate have been employed to validate the developed model. Furthermore, we have exploited the derived wave function to numerically reconstruct the wave patterns observed in microwave resonators and VCSELs. The

nice reconstruction not only manifests the importance of the resonant modes in interpreting the experimental results but also distinguish the resonant modes from the eigenmodes in the bound-state problems.

ACKNOWLEDGMENT

The authors acknowledge the National Science Council of Taiwan for their financial support of this research under Contract No. NSC-100-2628-M-009-001-MY3.

-
- [1] H. Nowakowska, M. Jasiński, and J. Mizeraczyk, *Eur. Phys. J. D* **54**, 511 (2009).
 - [2] A. W. Leissa, *Vibration of Plates* (Acoustical Society of America, Melville, NY, 1993).
 - [3] T. H. Lu, Y. C. Lin, Y. F. Chen, and K. F. Huang, *Opt. Express* **17**, 3007 (2009).
 - [4] T. H. Lu, Y. C. Lin, Y. F. Chen, and K. F. Huang, *Appl. Phys. B* **103**, 991 (2011).
 - [5] R. W. Robinett, *Quantum Mechanics: Classical Results, Modern Systems, and Visualized Examples* (Oxford University Press, New York, 1997).
 - [6] D. L. Kaufman, I. Kosztin, and K. Schulten, *Am. J. Phys.* **67**, 133 (1999).
 - [7] P. Amore, *J. Phys. A: Math. Theor.* **41**, 265206 (2008).
 - [8] D. D. de Menezes, M. Jar e Silva, and F. M. de Aguiar, *Chaos* **17**, 023116 (2007).
 - [9] S. Sridhar, *Phys. Rev. Lett.* **67**, 785 (1991).
 - [10] J. Stein and H.-J. Stöckmann, *Phys. Rev. Lett.* **68**, 2867 (1992).
 - [11] K. Schaad, T. Guhr, C. Ellegaard, and M. Oxborow, *Phys. Rev. E* **68**, 036205 (2003).
 - [12] A. Kudrolli, M. C. Abraham, and J. P. Gollub, *Phys. Rev. E* **63**, 026208 (2001).
 - [13] K. F. Huang, Y. F. Chen, H. C. Lai, and Y. P. Lan, *Phys. Rev. Lett.* **89**, 224102 (2002).
 - [14] T. Gensty, K. Becker, I. Fischer, W. Elsäßer, C. Degen, P. Debernardi, and G. P. Bava, *Phys. Rev. Lett.* **94**, 233901 (2005).
 - [15] M. D. Waller, *Proc. Phys. Soc. London* **50**, 77 (1938).
 - [16] M. D. Waller, *Proc. Phys. Soc. London* **52**, 452 (1940).
 - [17] Y. F. Chen, K. F. Huang, H. C. Lai, and Y. P. Lan, *Phys. Rev. Lett.* **90**, 053904 (2003).
 - [18] U. Kuhl, E. Persson, M. Barth, and H.-J. Stöckmann, *Eur. Phys. J. B* **17**, 253 (2000).
 - [19] I. V. Zozoulenko and K.-F. Berggren, *Phys. Rev. B* **56**, 6931 (1997).
 - [20] K. Schaad, A. P. B. Tufaile, and C. Ellegaard, *Phys. Rev. E* **67**, 026213 (2003).
 - [21] T. Tudorovskiy, R. Höhmann, U. Kuhl, and H. J. Stöckmann, *J. Phys. A: Math. Theor.* **41**, 275101 (2008).
 - [22] F. Lackner, I. Březinová, J. Burgdörfer, and F. Libisch, *Phys. Rev. E* **88**, 022916 (2013).
 - [23] H. J. Stöckmann, *Quantum Chaos—An Introduction* (Cambridge University Press, Cambridge, 1999).
 - [24] O. Bohigas, M. J. Giannoni, and C. Schmit, *Phys. Rev. Lett.* **52**, 1 (1984).
 - [25] E. Ventsel and T. Krauthammer, *Thin Plates and Shells* (Dekker, New York, 2004).
 - [26] N. A. Loiko and I. V. Babushkin, *J. Opt. B* **3**, S234 (2001).
 - [27] I. V. Babushkin, N. A. Loiko, and T. Ackemann, *Phys. Rev. E* **69**, 066205 (2004).
 - [28] N. Savitskyy, O. Hul, and L. Sirk, *Phys. Rev. E* **70**, 056209 (2004).
 - [29] O. Hul, N. Savitskyy, O. Tymoshchuk, S. Bauch, and L. Sirk, *Phys. Rev. E* **72**, 066212 (2005).
 - [30] P. H. Tuan, Y. T. Yu, P. Y. Chiang, H. C. Liang, K. F. Huang, and Y. F. Chen, *Phys. Rev. E* **85**, 026202 (2012).
 - [31] A. Molitor, M. Blazek, and W. Elsäßer, *Opt. Lett.* **36**, 3777 (2011).
 - [32] J. A. Hudgings, S. F. Lim, G. S. Li, W. Yuen, K. Y. Lau, and C. J. Chang-Hasnain, *IEEE Photon. Technol. Lett.* **11**, 245 (1999).
 - [33] S. P. Hegarty, G. Huyet, J. G. McInerney, and K. D. Choquette, *Phys. Rev. Lett.* **82**, 1434 (1999).
 - [34] I. V. Babushkin, M. Schulz-Ruhtenberg, N. A. Loiko, K. F. Huang, and T. Ackemann, *Phys. Rev. Lett.* **100**, 213901 (2008).
 - [35] C. C. Chen, K. W. Su, T. H. Lu, C. C. Liu, Y. F. Chen, and K. F. Huang, *Phys. Rev. E* **76**, 026219 (2007).
 - [36] Y. F. Chen, K. F. Huang, H. C. Lai, and Y. P. Lan, *Phys. Rev. E* **68**, 026210 (2003).
 - [37] J. D. Jackson, *Classical Electrodynamics* (Wiley, New York, 1975), Chap. 8.